

Supporting Information

for

Second-Sphere Effects in Dinuclear Fe^{III}Zn^{II} Hydrolase Biomimetics: Tuning Binding and Reactivity Properties

Tiago Pacheco Camargo,[†] Ademir Neves,^{*,†} Rosely A. Peralta,[†] Cláudia Chaves,[†] Elene C. P. Maia,^{||} Edgar H. Lizarazo-Jaimes,^{||} Dawidson A. Gomes,[⊥] Tiago Bortolotto,[#] Douglas R. Norberto,[#] Hernán Terenzi,^{*,#} David L. Tierney,[‡] Gerhard Schenk.[§]

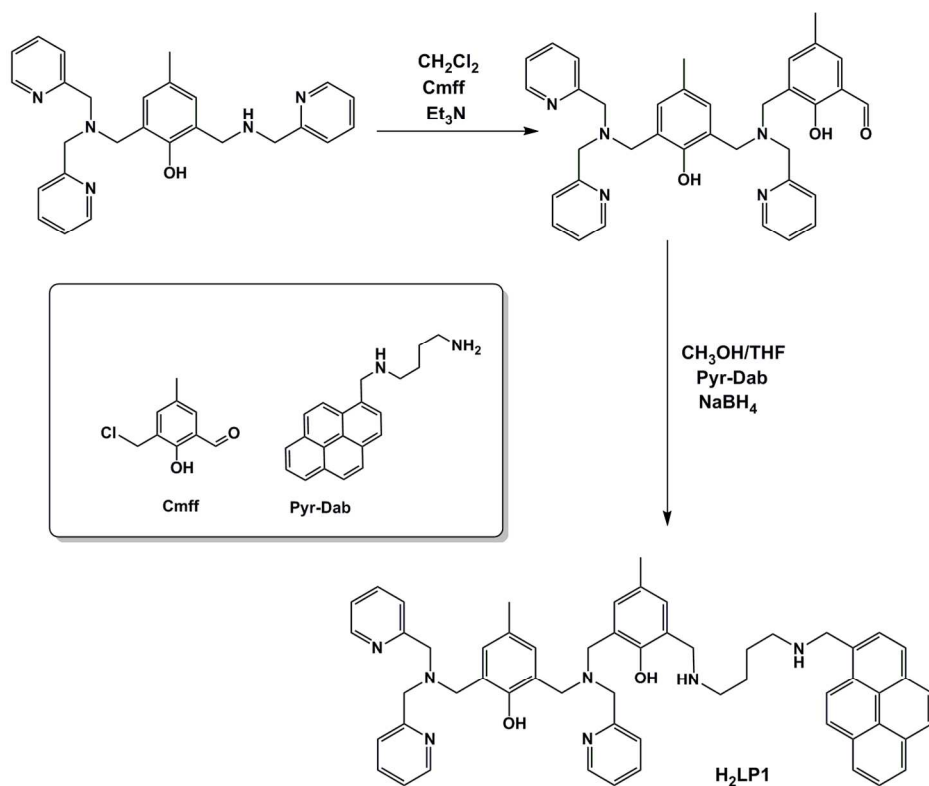
[†]Departamento de Química - LABINC, and [#]Departamento de Bioquímica – CEBIME, Universidade Federal de Santa Catarina, 88040-900 Florianópolis-SC, Brazil,

^{||}Departamento de Química, and [⊥]Departamento de Bioquímica, Universidade Federal de Minas Gerais, Belo Horizonte, MG, 31270-901, Brazil,

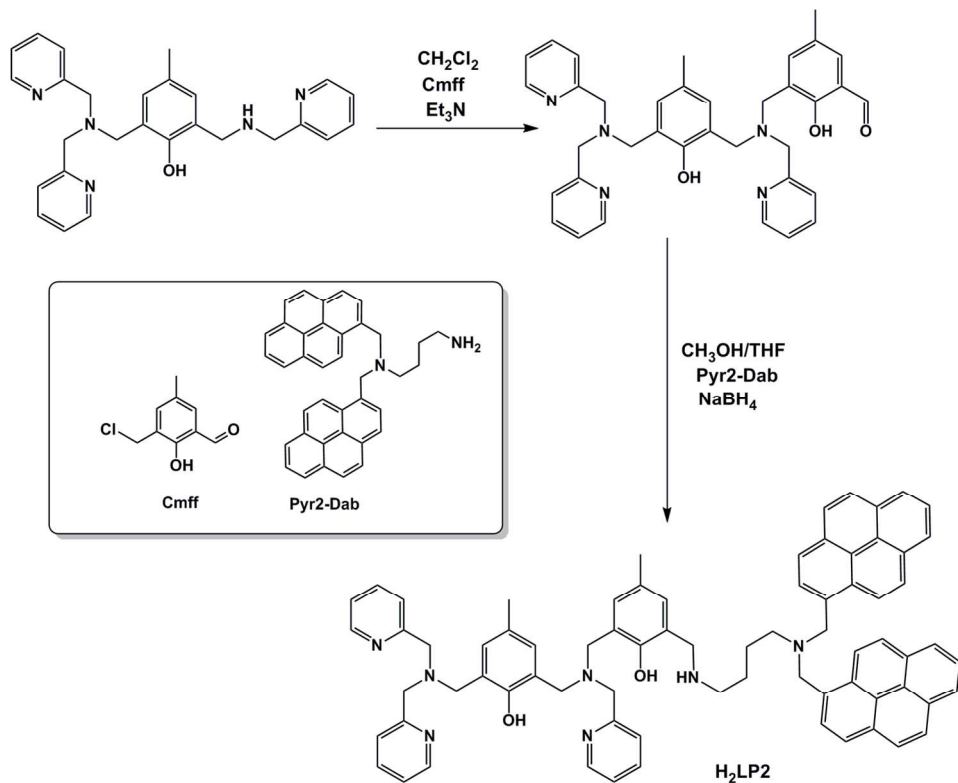
[‡]Department of Chemistry and Biochemistry, Miami University, Oxford, OH 45056 U.S.A.,

[§]School of Chemistry and Molecular Biosciences, The University of Queensland, Brisbane 4072, Australia.

Keywords: Metalloenzymes; biomimetics; hydrolase; DNA intercalator; chemotherapeutics.



Scheme S1. Synthesis of unsymmetrical ligand H_2LP1 .



Scheme S2. Synthesis of unsymmetrical ligand H_2LP2 .

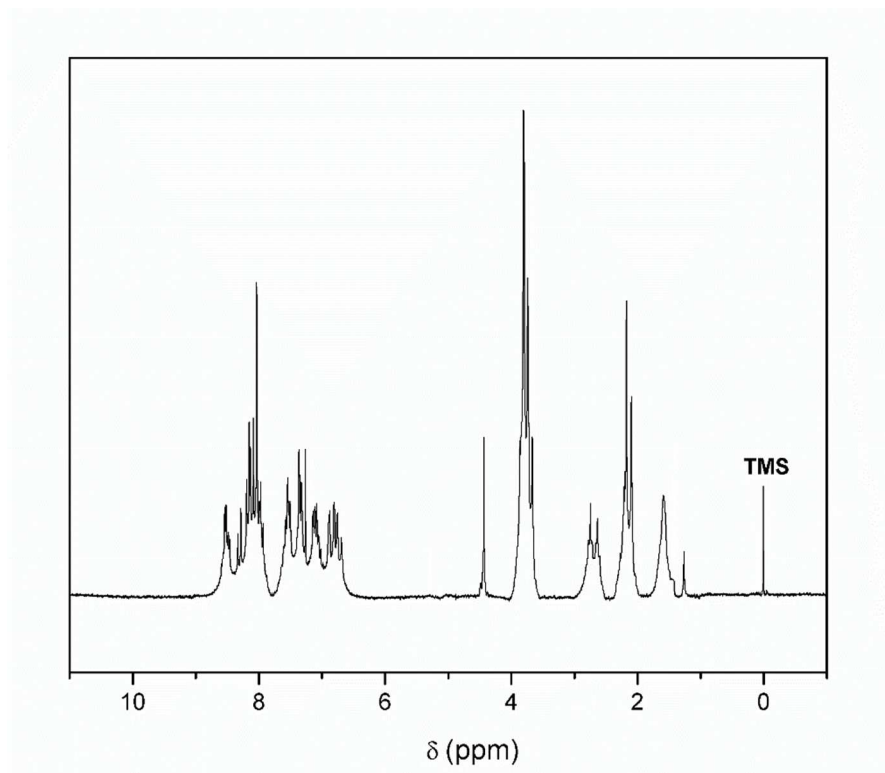


Figure S1. ^1H -NMR spectrum for the ligand $\text{H}_2\text{LP1}$ in CDCl_3 .

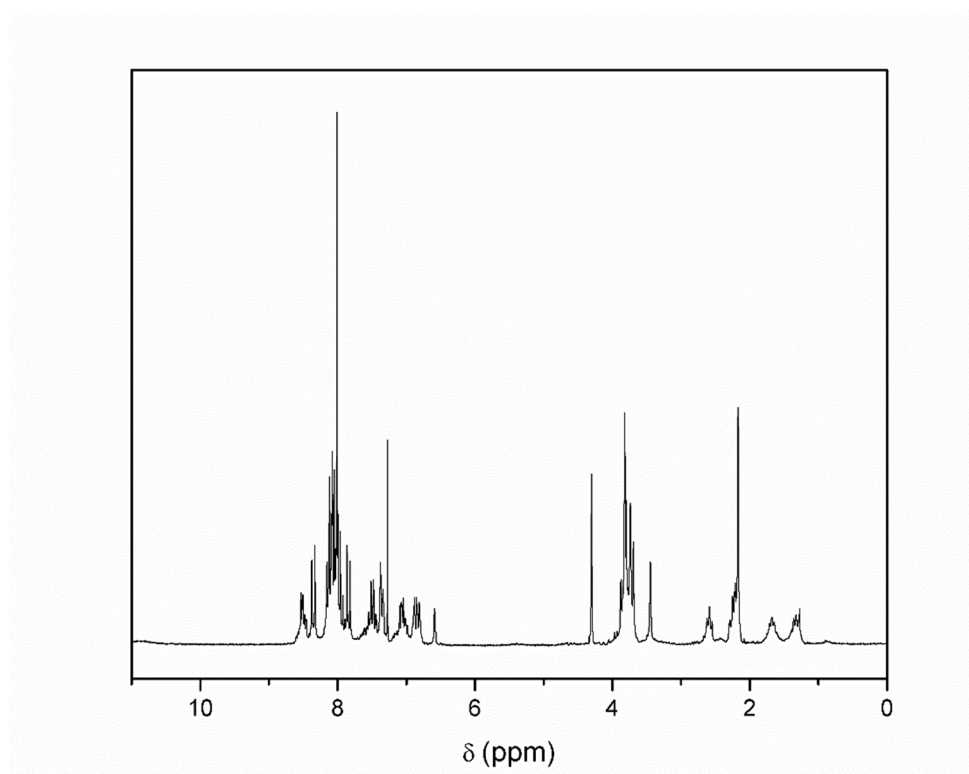


Figure S2. ^1H -NMR spectrum for the ligand $\text{H}_2\text{LP2}$ in CDCl_3 .

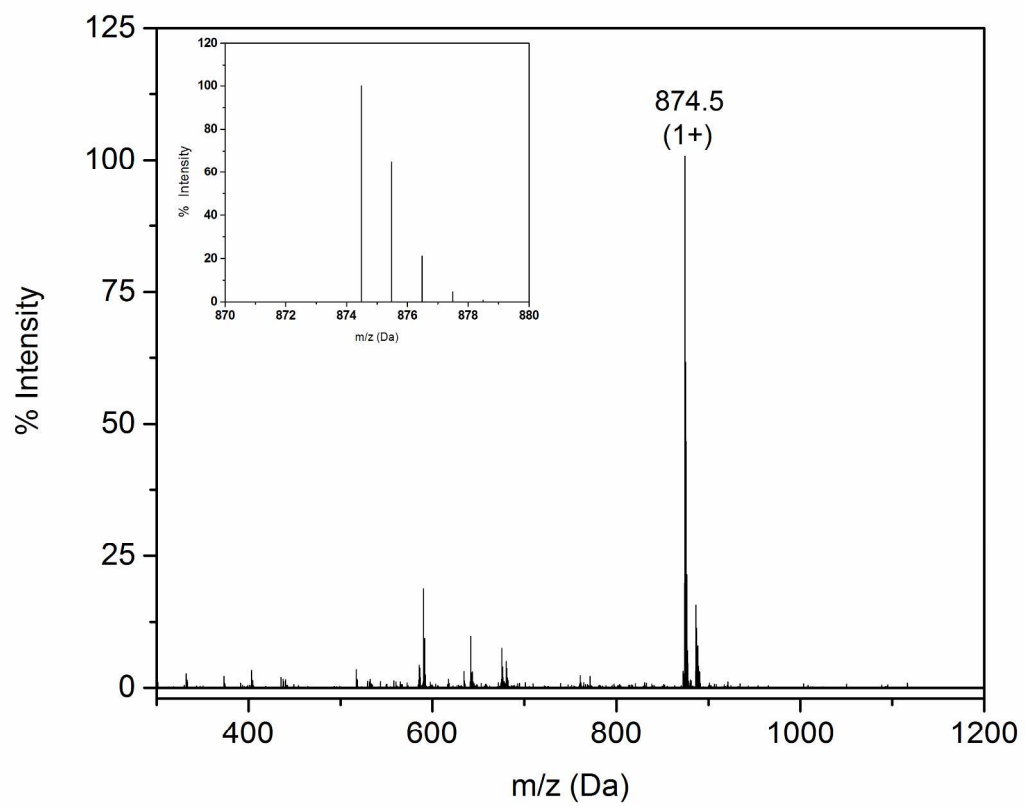


Figure S3. ESI-MS Positive ion spectra for the ligand H₂LP1.

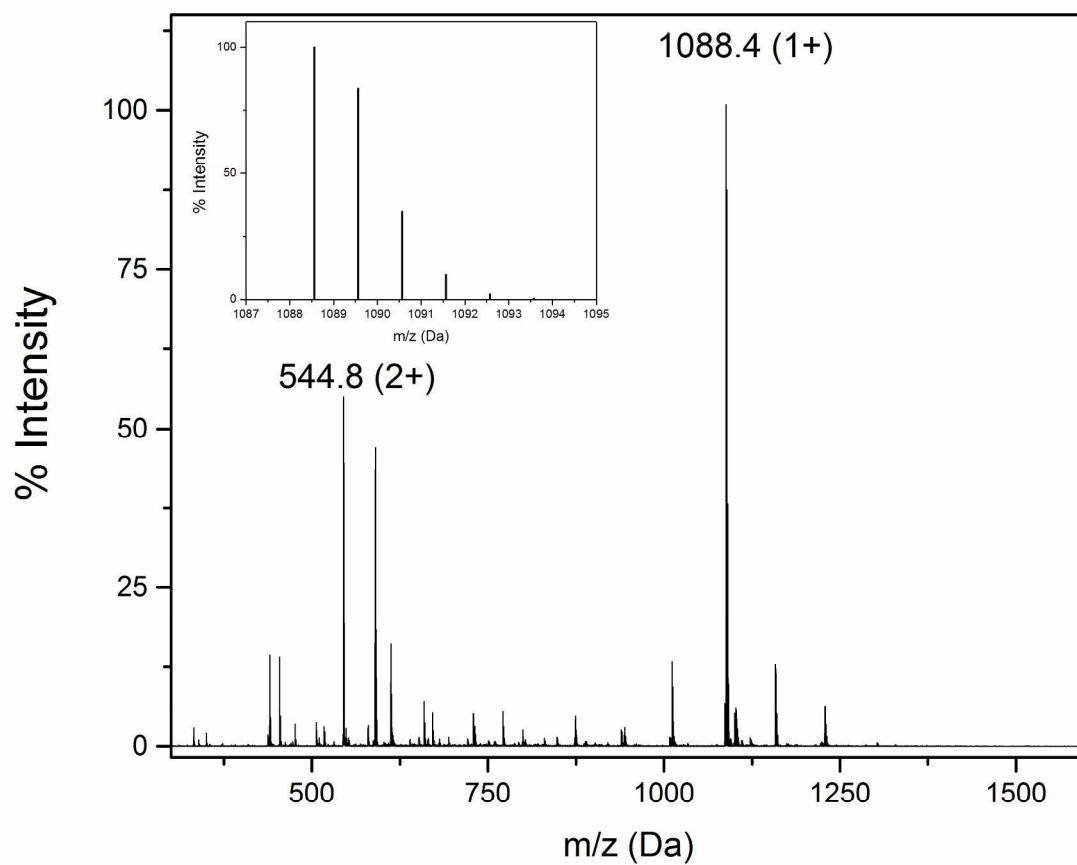


Figure S4. ESI-MS Positive ion spectra for the ligand H₂LP₂.

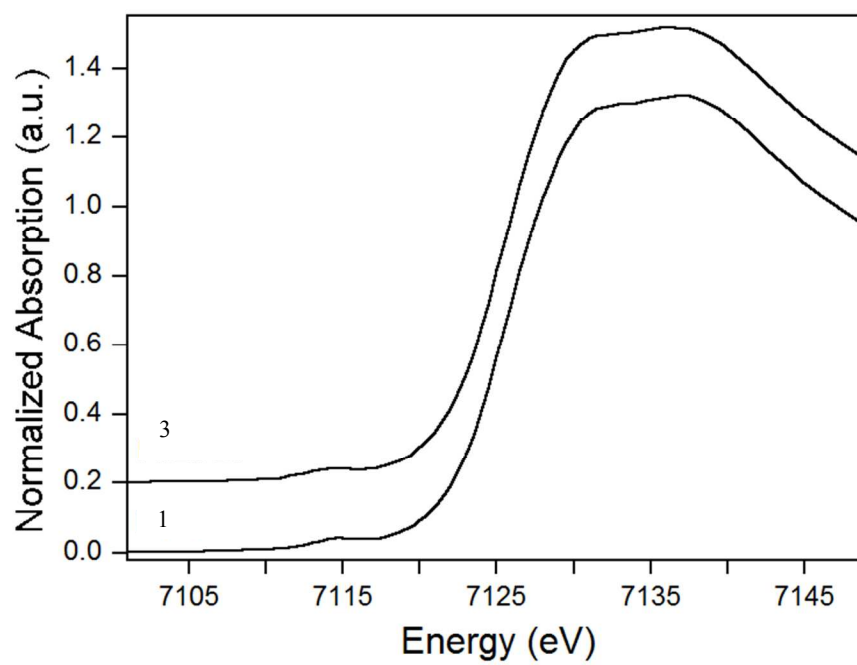


Figure S5. Fe XANES of (3) and (1).

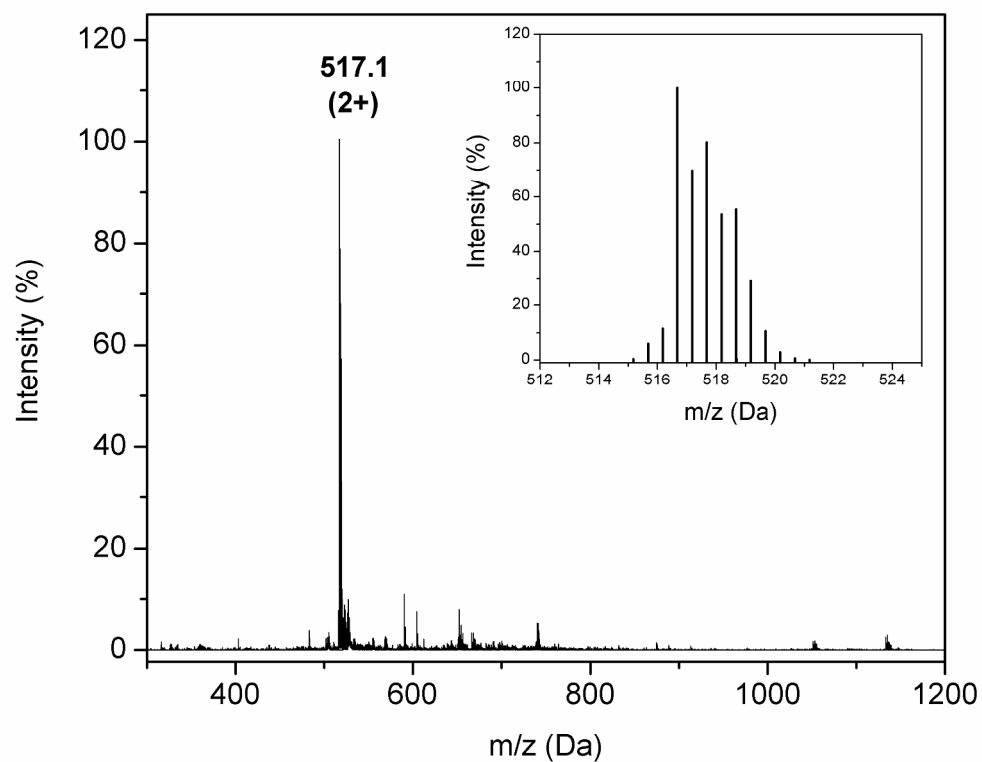


Figure S6. ESI-MS Positive ion spectra for the complex (1).

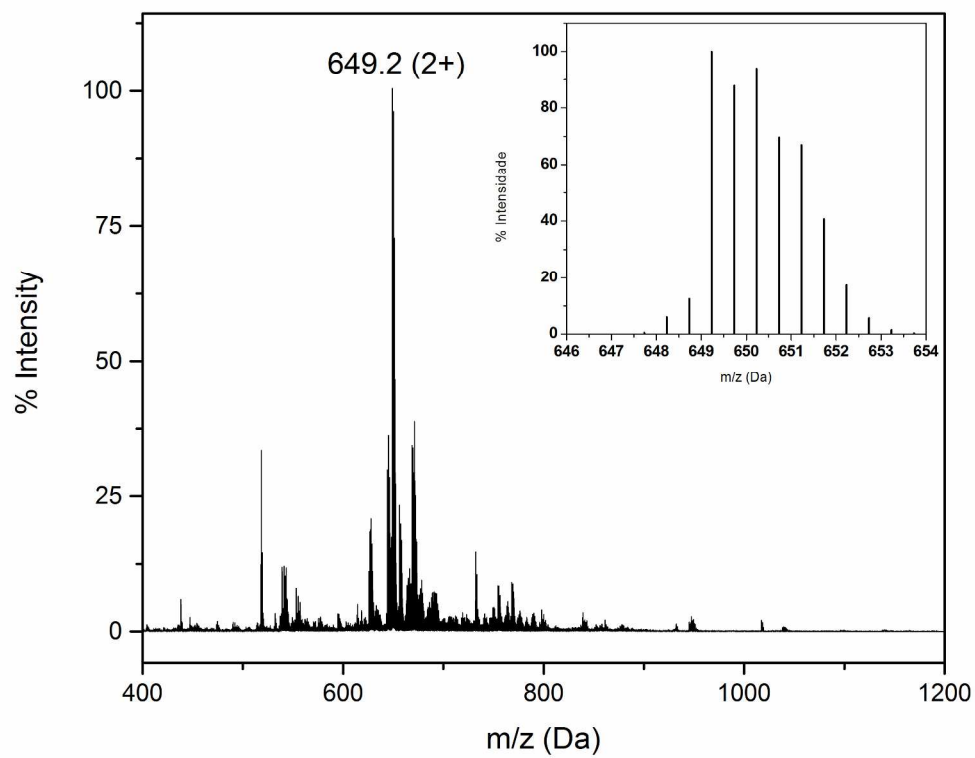


Figure S7. ESI-MS Positive ion spectra for the complex (2).

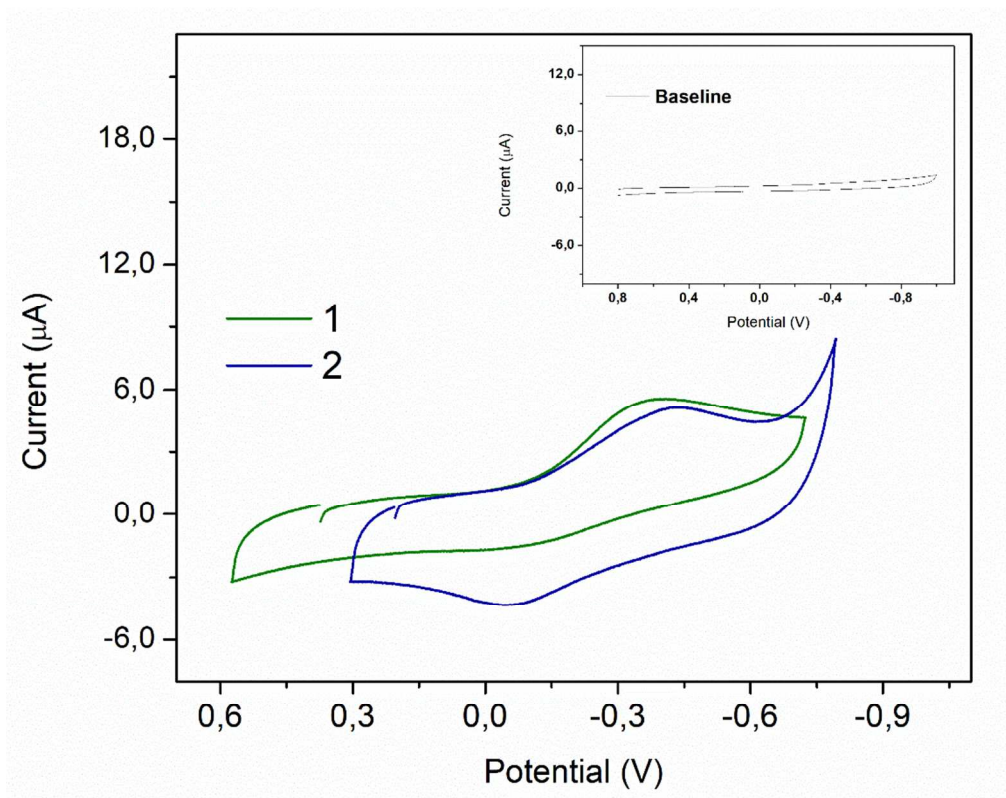


Figure S8. Cyclic voltammograms for complexes (1) (green) and (2) (blue) in acetonitrile/water (2:1). Conditions: $I = 0.1 \text{ M NaBF}_4$; carbon working electrode, platinum wire auxiliary electrode, reference: Ag/Ag^+ ; internal standard: $\text{K}_3[\text{Fe}(\text{CN})_6]$.

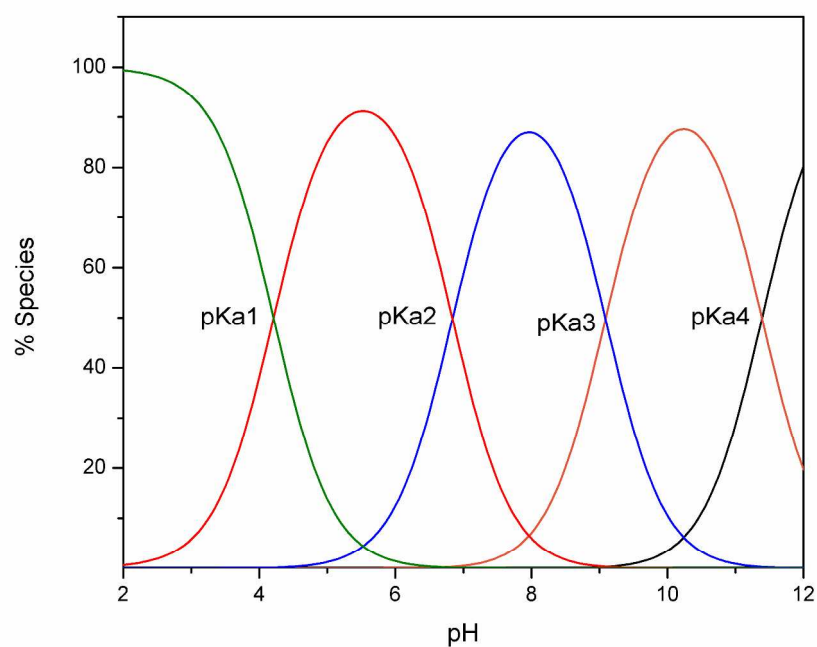


Figure S9. Distribution Species Graph for complex (1).

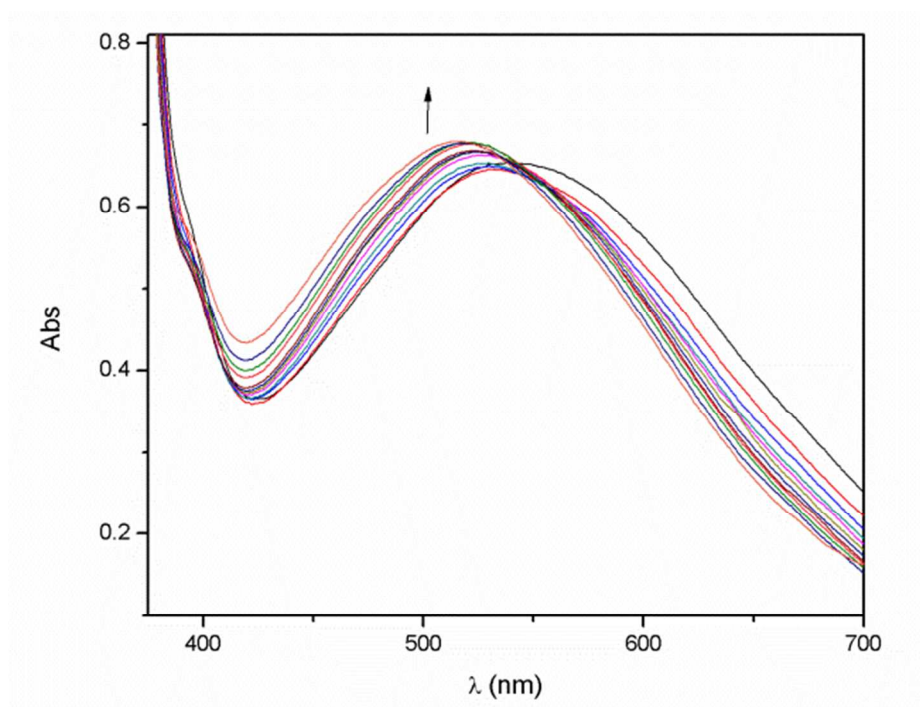


Figure S10. Spectrophotometric titration for complex **(2)** in acetonitrile/water (2:1). Conditions $[2] = 200 \mu\text{M}$; $I = 0.1 \text{ M NaClO}_4$.

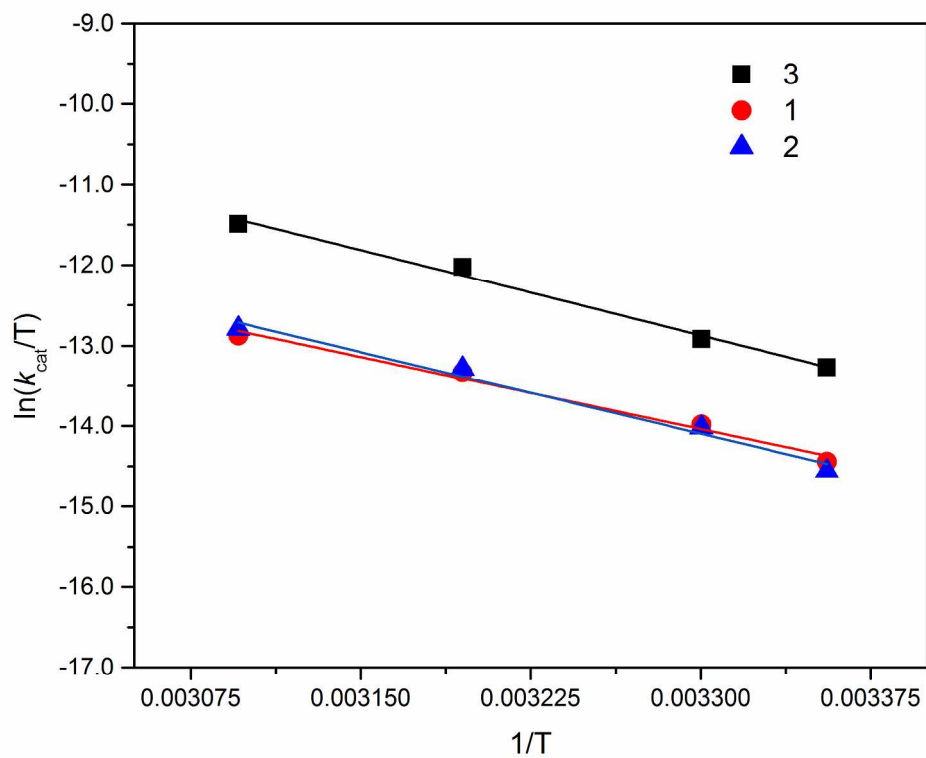


Figure S11. Eyring plot for complexes **(3)**, **(1)** and **(2)**.

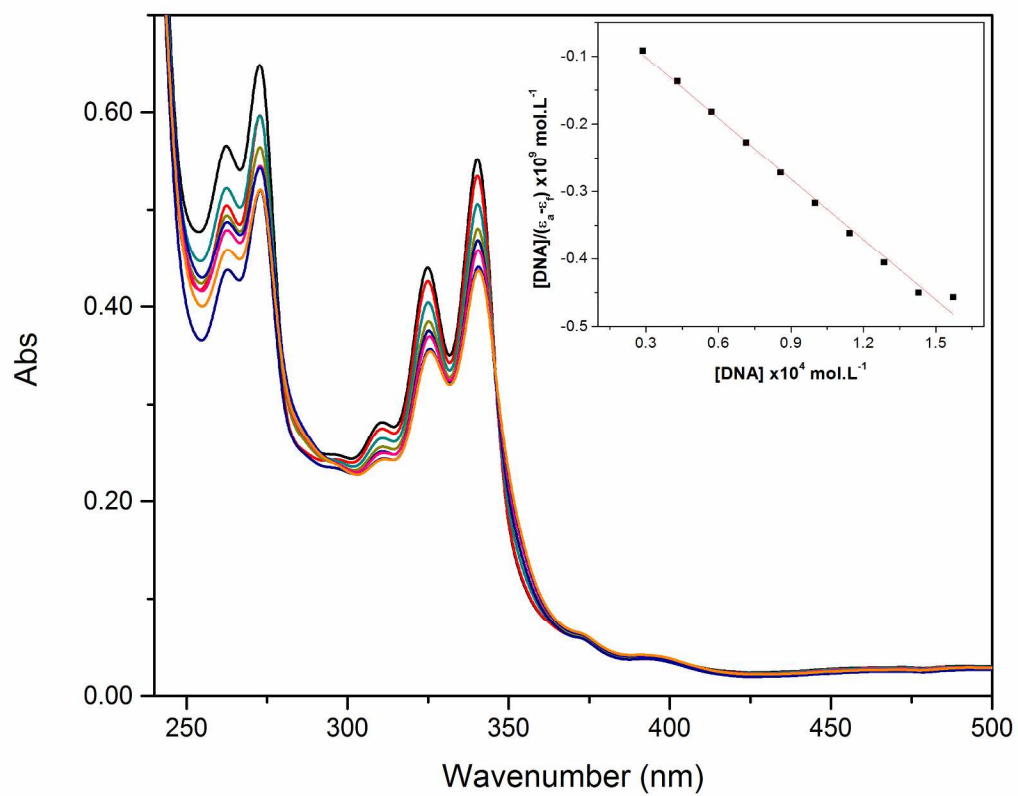


Figure S12. Spectrophotometric titration of (**1**) with increasing concentrations of CT-DNA at pH 7.0.

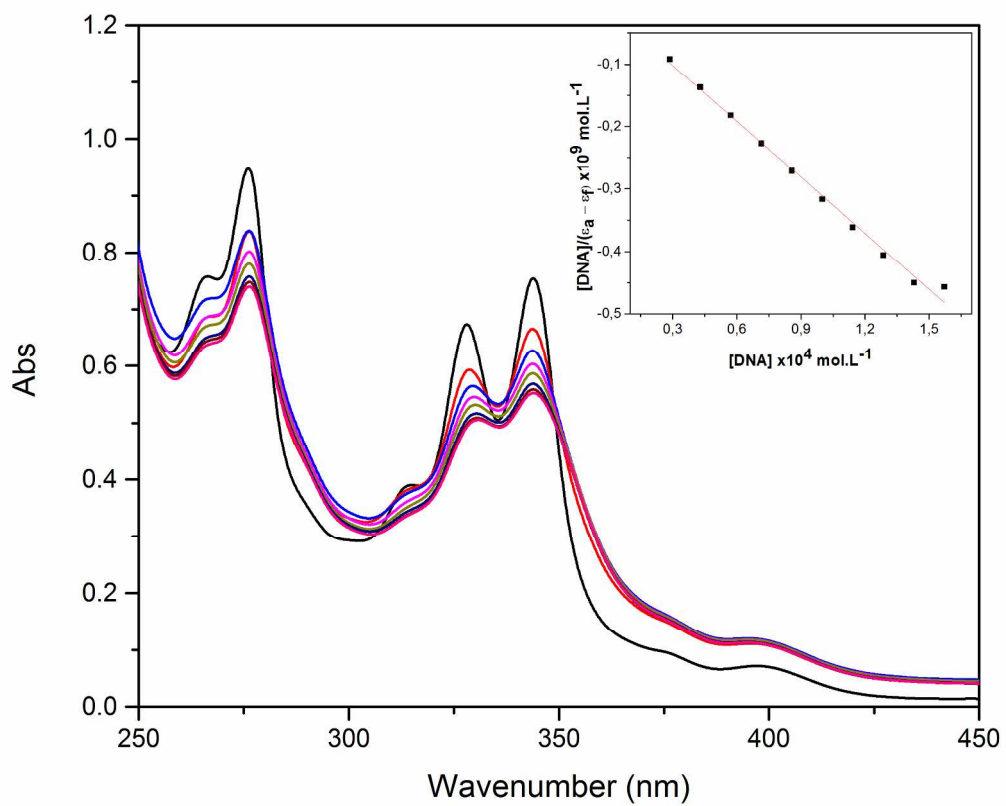


Figure S13. Spectrophotometric titration for (**2**) with increasing concentrations of CT-DNA at pH 7.0.

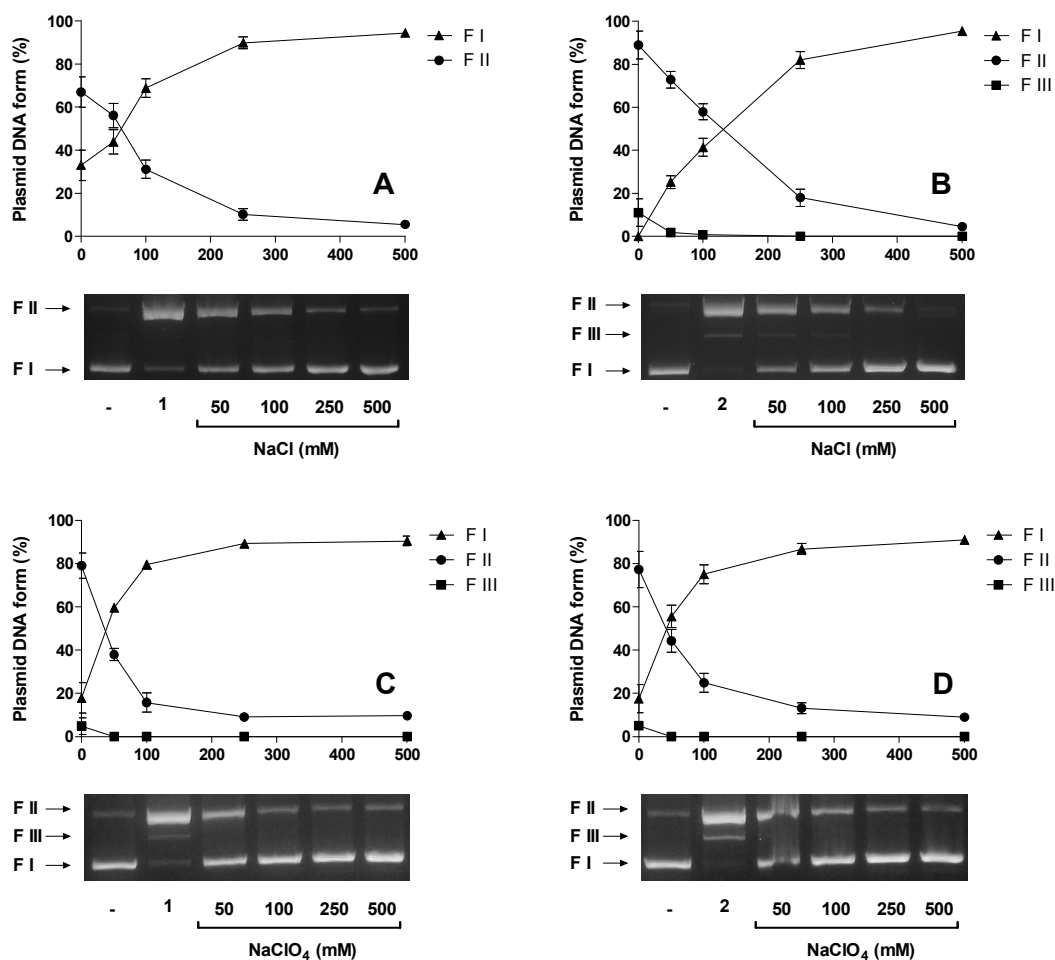


Figure S14. Effect of ionic strength on cleavage of plasmid DNA by (1) (A, NaCl; and C, NaClO₄) and (2) (B, NaCl; and D, NaClO₄) at 5 μ M for 16 h at 37 $^{\circ}$ C in 10 mM of HEPES buffer (pH 7.0). Results expressed as mean \pm standard deviation obtained from three independent experiments.

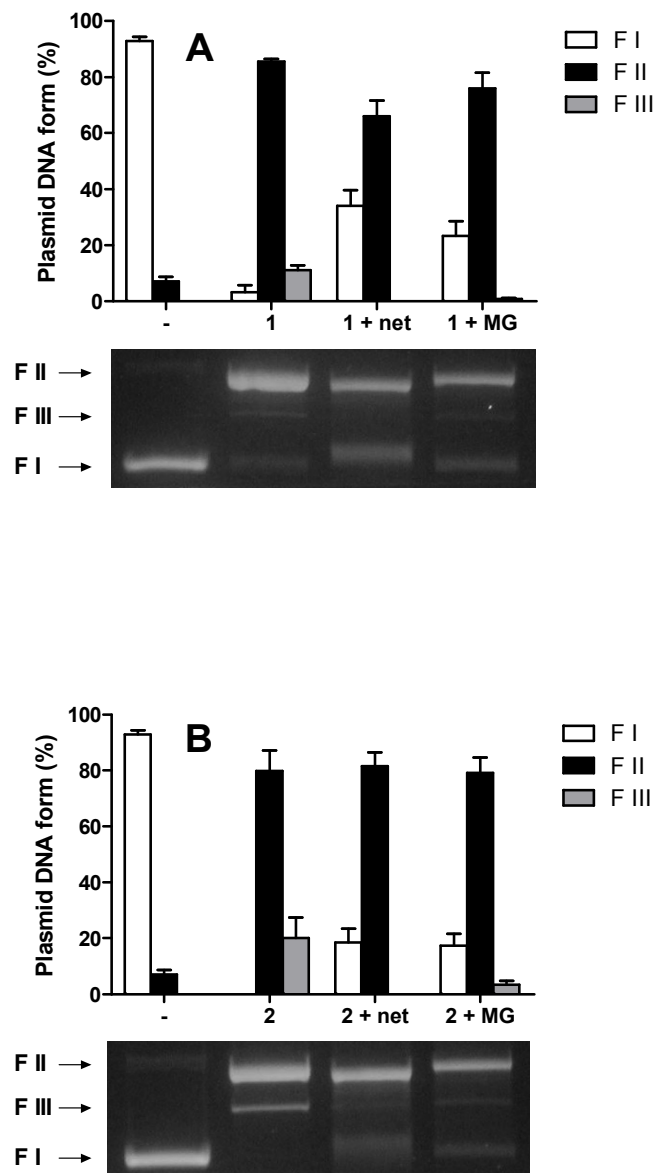


Figure S15. Effect of DNA groove binders netropsin (net, 50 μ M) and methyl green (MG, 50 μ M) on plasmid DNA cleavage by 5 μ M of (1) (A) and (2) (B) for 16 h at 37 $^{\circ}$ C in 10 mM of HEPES buffer (pH 7.0). Results are expressed as mean values \pm standard deviations obtained from three independent experiments.

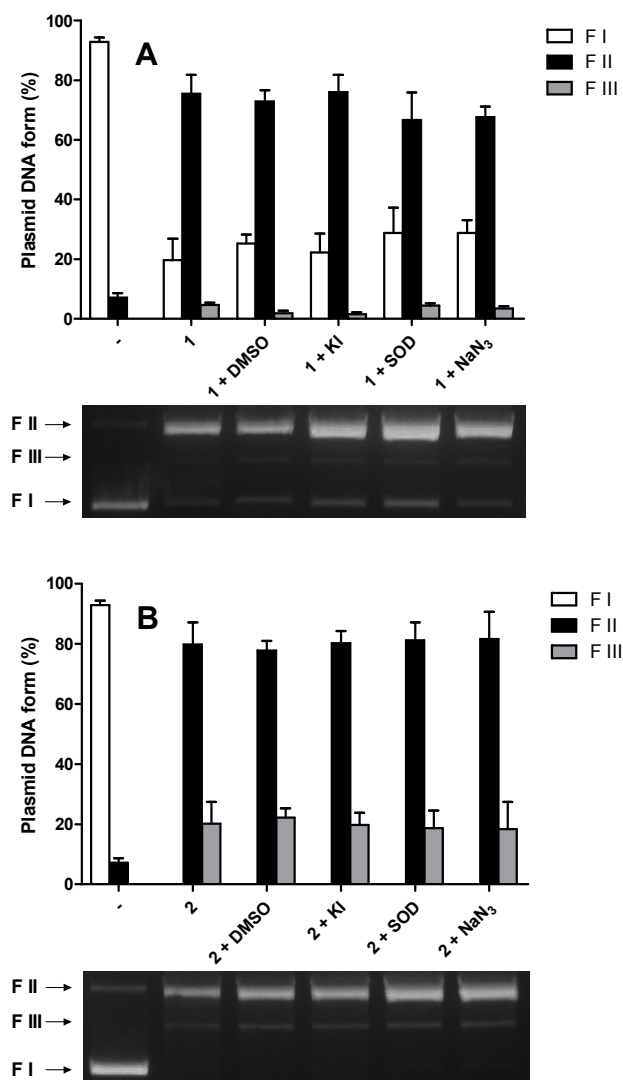


Figure S16. Effect of ROS scavengers on the cleavage of plasmid DNA in the presence of 5 μ M (1) (A) or (2) (B) for 16 h at 37 $^{\circ}$ C in 10 mM of HEPES buffer (pH 7.0). The ROS scavengers used were DMSO (10%), KI (0.5 mM), SOD (20 units) and NaN_3 (0.5 mM). The controls (reactions without complex) for each inhibitor showed DNA cleavage similar to or even lower than the controls presented in the figures (data not shown). Results are expressed as mean values \pm standard deviations from three independent experiments.

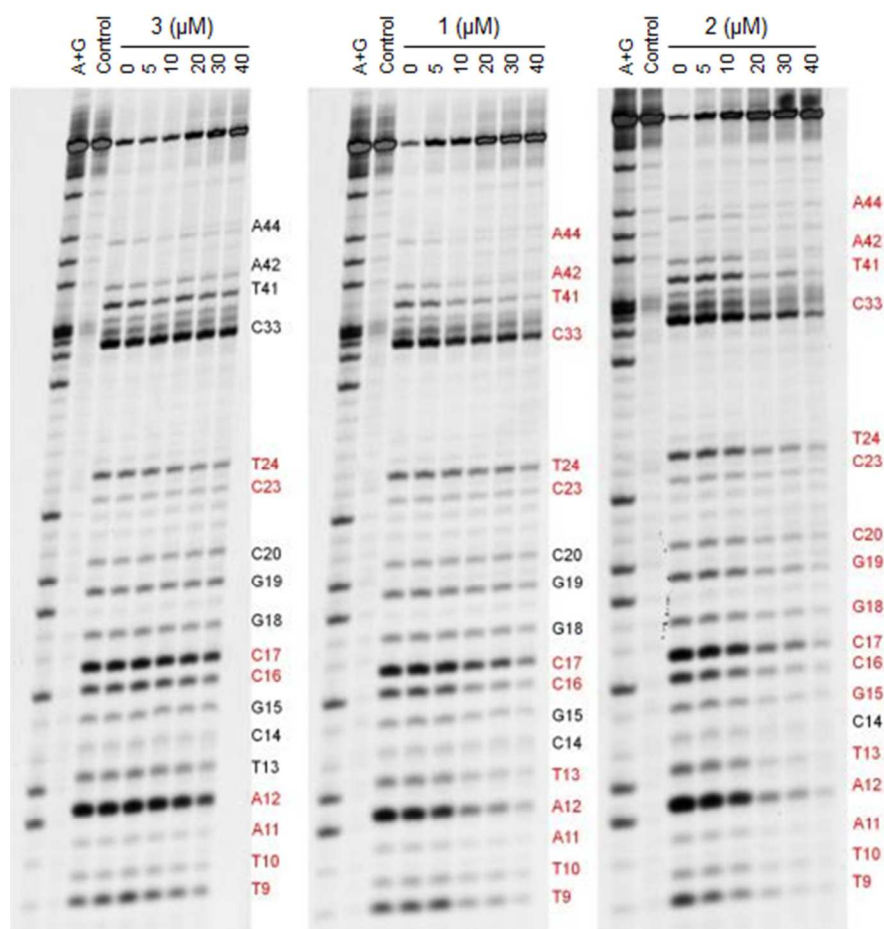
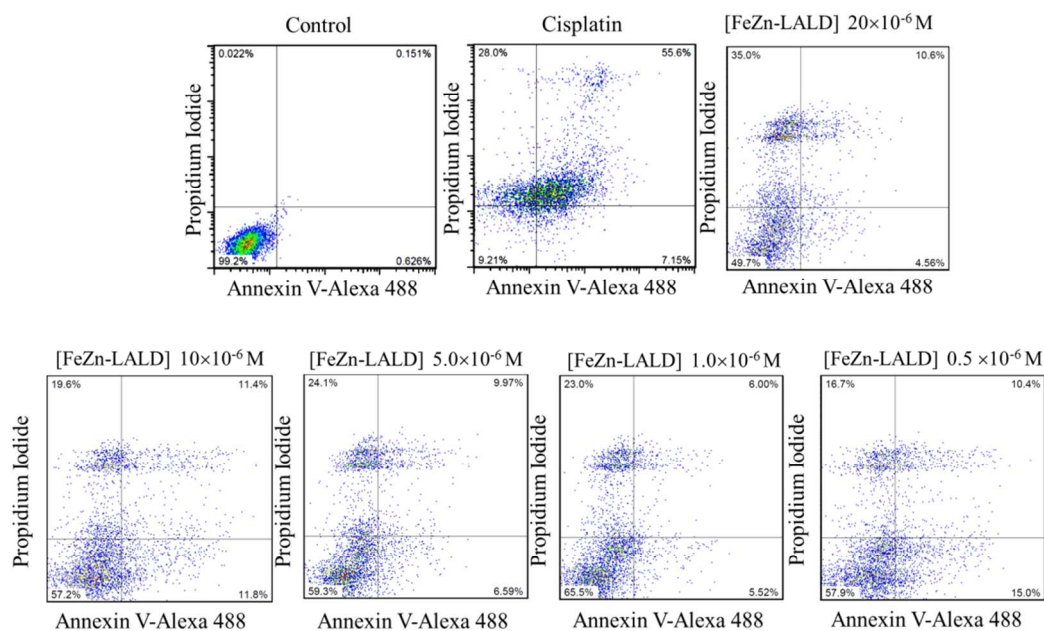


Figure S17. DNAse I footprinting titration of (3), (1) and (2) (0 to 40 μM) on the 49-mer substrate. A+G ladder represents the Maxam-Gilbert Adenine + Guanine specific cleavage by formic acid modification followed by hot piperidine treatment. The positions noted represent the fragments generated by DNase I digestion and the red text indicates the sites protected by the titrated complexes.

(A)



(B)

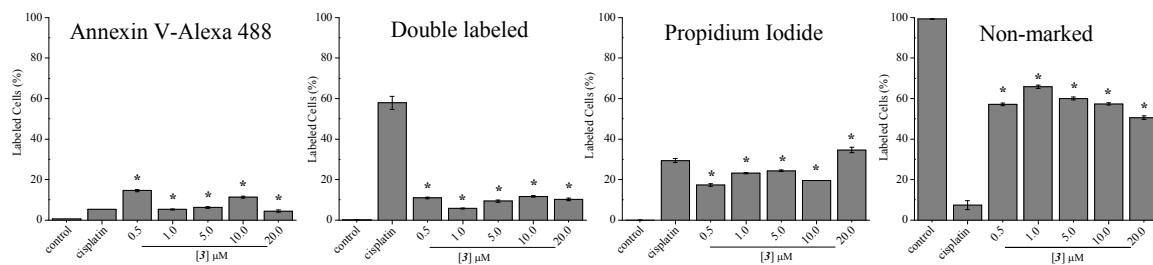
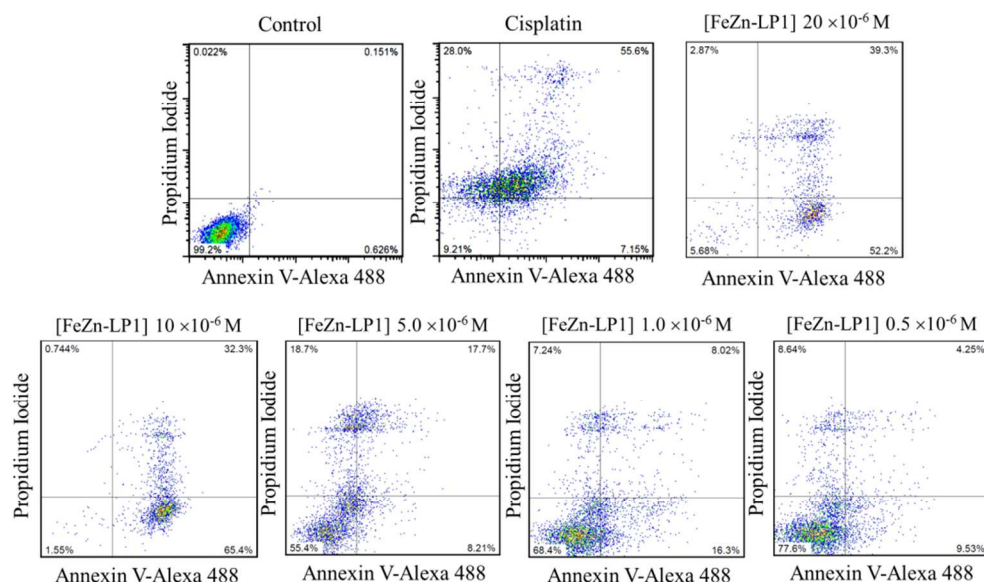


Figure S18. Induction of apoptosis by complex (3). Annexin V-Alexa 488 and propidium iodide fluorescence were measured by flow cytometry. (A) Representative dot plots of dose-dependent effect of complex (3) on apoptosis in K562 cells treated for 24 h. A total of 5000 events were collected per sample. (B) The bar graphs show the cell labeled with Annexin V-Alexa 488 and/or propidium iodide and unlabeled (right). Mean concentrations were compared between groups by one-way ANOVA and the Bonferroni multiple comparison test ($n=3$; $*P < 0.05$). Cisplatin at $10 \mu\text{mol L}^{-1}$ was used as a positive control. The values are the mean of triplicate determinations.

(A)



(B)

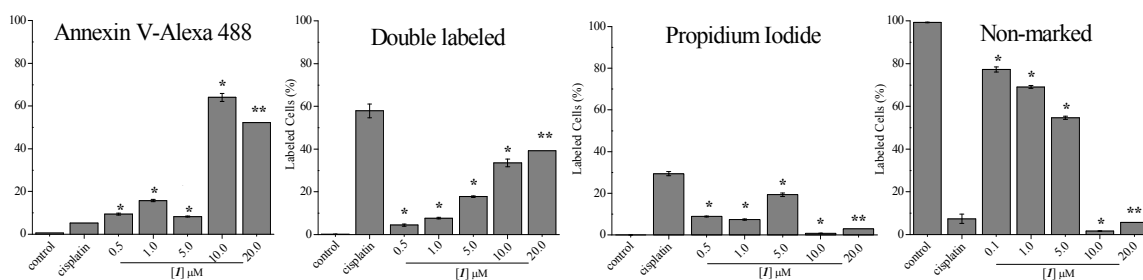


Figure S19. Induction of apoptosis by complex (1). Annexin V-Alexa 488 and propidium iodide fluorescence were measured by flow cytometry. (A) Representative dot plots of dose-dependent effect of complex (1) on apoptosis in K562 cells treated for 24 h. A total of 5000 events were collected per sample. (B) The bar graphs show the cell labeled with Annexin V-Alexa 488 and/or propidium iodide, and unlabeled (right). Mean concentrations were compared between groups by one-way ANOVA and the Bonferroni multiple comparison test ($n=3$; * $P < 0.05$, ** $n < 3$). Cisplatin at 10 μ M was used as a positive control. The values are the mean of triplicate determinations.